



One-dimensional covalent organic frameworks with atmospheric water harvesting for photocatalytic hydrogen evolution from water vapor

Yong Liu^a, Wang-Kang Han^a, Wenwen Chi^a, Jia-Xing Fu^a, Yuqian Mao^a, Xiaodong Yan^a, Jun-Xiang Shao^a, Yuqin Jiang^b, Zhi-Guo Gu^{a,*}

^a Key Laboratory of Synthetic and Biological Colloids, Ministry of Education, School of Chemical and Material Engineering, Jiangnan University, Wuxi 214122, PR China

^b Henan Engineering Research Centre of Chiral Hydroxyl Pharmaceutical, School of Chemistry and Chemical Engineering, Henan Normal University, Xinxiang 453007, PR China

ARTICLE INFO

Keywords:

One-dimensional
Covalent organic frameworks
Atmospheric water harvesting
Water vapor splitting
Photocatalytic hydrogen

ABSTRACT

Photocatalytic hydrogen evolution from water vapor presents a novel approach to solar energy conversion. Nevertheless, the design and synthesis of water-adsorbing photocatalysts is exceedingly challenging. In this report, we for the first time present three hygroscopic one-dimensional (1D) covalent organic frameworks (COFs) based on photosensitive pyrene (Py-MPA, Py-PDCA, and Py-HMPA) combined with atmospheric water harvesting (AWH) and photocatalysis for photocatalytic water vapor splitting. Due to the ultra-small pores of the 1D structure, with hydrophilic -OH sites satisfying the microporous filling of water molecules, Py-HMPA demonstrated superior water adsorption capacity at lower humidity. Remarkably, Py-HMPA exhibited an impressive H₂ production rate of 105 μmol g⁻¹ h⁻¹ and high stability during solid-state photocatalysis utilizing water vapor. Overall, this work paves a new pathway of organic porous materials for photocatalytic water vapor splitting.

1. Introduction

Photocatalytic water splitting for H₂ production is recognized as the most effective solution for energy crises and environmental challenges [1–3]. In most cases, the photocatalytic H₂ evolution was carried out in liquid water. However, this method faces several challenges such as the demanding reaction system, the decomposition of photocatalyst, and the possible icing disrupted reaction [4,5]. In contrast, photocatalytic H₂ production by splitting water vapor provides greater scalability, but the requirement of combining water vapor adsorption in photocatalysts is an extremely challenging task [6–8]. Therefore, current research on photocatalytic H₂ production from water vapor focused on inorganic photocatalyst composites composed of water absorbers, which show inferior performance and limiting practical applications due to low water vapor adsorption and inefficient light harvesting [4,9–11].

Covalent organic frameworks (COFs) have recently emerged as a new generation of crystalline organic semiconductors. The energy band and reactive sites of COFs could be engineered at molecular level, and the crystalline conjugated structure could prevent the recombination of photogenerated electrons and holes [12–18]. COFs also have been demonstrated as promising atmospheric water harvesting (AWH)

materials due to its large specific surface area, diverse pore volume, tunable structure and good stability [19–22]. Therefore, it is feasible for COFs to simultaneously realize both AWH and photocatalysis for photocatalytic water vapor splitting to produce H₂.

To devise hygroscopic COFs for photocatalytic H₂ evolution using water vapor, the following considerations should be taken into account (Scheme 1): (i) the light-harvesting ability, appropriate band structure and rapid carrier separation are necessary for efficient photocatalysis; (ii) the presence of accessible hydrophilic sites, such as -OH and N of pyridine, where water molecules nucleate; (iii) the existence of uniform microporous channel that allows for rapid adsorption and transport of water molecules [23–27]. Unfortunately, conventional COFs are unable to achieve this uniform microporous channel. 1D COFs can be constructed using V-shaped C₂ connectors and planar C₄ connectors, resulting in a ribbon structure [28–30]. Importantly, the V-shaped C₂ connectors facilitate the creation of ultra-small pores, which enhance the micropore filling of AWH.

Herein, three hygroscopic pyrene-based 1D Py-COFs (Py-MPA, Py-PDCA and Py-HMPA) with ultra-small micropores were constructed by combining 4,4',4'',4'''-(pyrene-1,3,6,8-tetrayl)tetraaniline (Py-NH₂) with m-phthalaldehyde (MPA), 2,6-pyridinedicarboxaldehyde (PDCA)

* Corresponding author.

E-mail address: zhiguogu@jiangnan.edu.cn (Z.-G. Gu).

<https://doi.org/10.1016/j.apcatb.2023.123074>

Received 31 May 2023; Received in revised form 4 July 2023; Accepted 5 July 2023

Available online 7 July 2023

0926-3373/© 2023 Elsevier B.V. All rights reserved.

and 2-hydroxy-5-methylisophthalaldehyde (HMPA) through $120^\circ + 60^\circ$ strategy (Fig. 1a). Py-NH₂ was selected as the constitutive precursor owing to its well-established broad light absorption and appropriate energy bands. MPA, PDCA, and HMPA were utilized as non-linear connectors of 120° to regulate the water absorption sites. The investigations showed that Py-COFs displayed the anticipated AWH and photocatalytic performance. Furthermore, Py-HMPA with hydrophilic -OH groups exhibited an acceptable H₂ production rate of $105 \mu\text{mol g}^{-1} \text{h}^{-1}$ with high stability for photocatalytic H₂ evolution under water vapor. The electronegative -OH groups present in Py-HMPA not only enhanced the adsorption of water molecules but also improved the separation of carriers. To the best of our knowledge, this was the first successful combination of AWH and photocatalysis, as well as the first application of COFs for photocatalytic H₂ evolution from water vapor.

2. Experimental

A complete description of chemicals, materials, and instrumentations is available in the [Supporting Information](#).

2.1. Synthesis of Py-MPA

A Pyrex tube of 20×60 mm (o.d \times length) was charged with Py-NH₂ (28.0 mg, 0.05 mmol), MPA (13.4 mg, 0.1 mmol), 1-Butanol (1.4 mL) and 1, 2-Dichlorobenzene (0.6 mL). After sonication for 10 min, 0.2 mL of aqueous acetic acid (6 M) was added and sonicated for 10 min. The tube was flash frozen at 77 K (liquid N₂ bath), evacuated to an internal pressure of 50 mTorr and flame sealed. The reaction was heated at 120°C for 72 h. Then solids were filtered, washed with DMF, and transferred to a Soxhlet extractor and washed with THF (24 h). Finally, the product was evacuated at 120°C under vacuum overnight. Yield: 78%. Elemental analysis of Py-MPA: Calcd. for C₁₈₀N₁₂H₁₁₀: C, 59.61%; N, 3.97%; H, 36.42%.

2.2. Synthesis of Py-PDCA

Py-PDCA was synthesized following the same procedure as Py-MPA, replacing MPA with PDCA (13.5 mg, 0.1 mmol), and solvent with Mesitylene (1.4 mL) and 1,4-Dioxane (0.6 mL). Yield: 81%. Elemental analysis of Py-MPA: Calcd. for C₁₇₂N₂₀H₁₀₂: C, 58.50%; N, 6.80%; H, 34.70%.

2.3. Synthesis of Py-HMPA

Py-HMPA was synthesized following the same procedure as Py-PDCA, replacing PDCA with HMPA (16.4 mg, 0.1 mmol). Yield: 82%.

Elemental analysis of Py-HMPA: Calcd. for C₁₈₈N₁₂O₈H₁₂₆: C, 56.28%; N, 3.60%; O, 2.40%; H, 37.72%.

2.4. Photocatalytic H₂ production

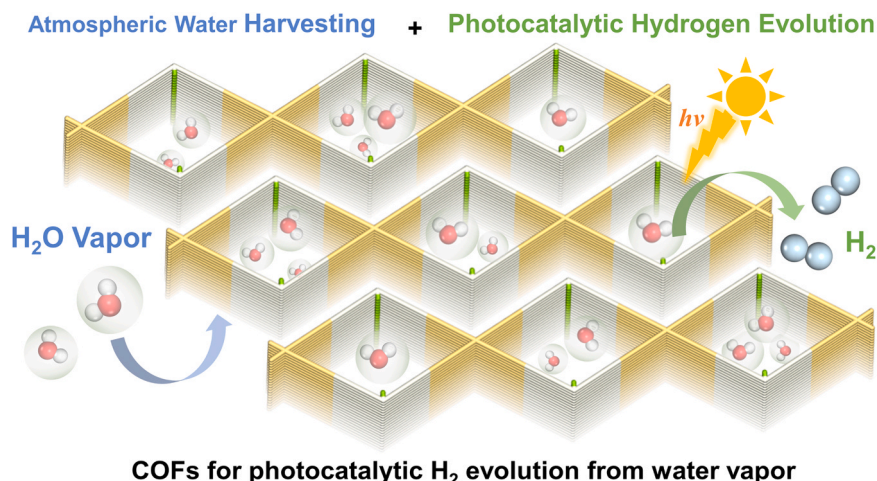
After the optimization conditions for photocatalytic H₂ evolution (Fig. S32), 5 mg of photocatalyst were suspended in 25 mL of H₂O containing 0.1 M ascorbic acid as the sacrificial agent, which was added into a hermetic device, primarily consisting of a quartz tube and sealing components. 7 wt% of Pt co-catalyst was loaded onto the photocatalyst through in-situ photo-deposition of H₂PtCl₆. Prior to the photocatalytic test, the device was purged with Ar flow to eliminate air. A 300 W Xenon lamp source (Beijing Perfectlight Technology Co., Ltd., Microsolar300) with a cutoff filter was employed to achieve visible light irradiation ($\lambda > 420$ nm, 100 mW cm^{-2}). The amount of H₂ produced was determined by gas chromatography. Cycling photocatalytic tests were conducted in the same manner after collecting and washing the samples with water.

3. Results

3.1. Synthesis and characterization

Py-MPA, Py-PDCA and Py-HMPA were synthesized via Schiff-base reaction of Py-NH₂ with MPA, PDCA and HMPA, respectively, with the presence of 6 M aqueous acetic acid at 120°C for 72 h. The as-synthesized Py-COFs were first characterized by FT-IR spectroscopy. The stretching vibration band around 1620 cm^{-1} illustrated the generation of C=N linkers (Fig. S9). Meanwhile, the vibrational bands at around $3300\text{--}3600 \text{ cm}^{-1}$ were ascribed to the vibration of water molecules, which demonstrated the ability of Py-COFs for AWH. The ¹³C solid-state NMR spectra further verified the formation of the C=N bonds with the characteristic signal at 160, 159, and 161 ppm for Py-MPA, Py-PDCA and Py-HMPA, respectively (Figs. S10–S12).

The crystallinity and structure of the Py-COFs were analyzed by powder X-ray diffraction (PXRD) measurements combined with structural simulations. The PXRD pattern of the Py-COFs exhibited nearly identical diffraction peaks, a predominant diffraction peak at $\sim 5.9^\circ$ with other weak peaks at $\sim 9.1^\circ$, $\sim 14.5^\circ$ and $\sim 24.3^\circ$, which could be assigned to the (110), (310), (420) and (001) planes, respectively (Fig. 1b–d). Considering the geometry and connection patterns of precursors, only three possible structures for Py-COFs were expected according to Reticular Chemistry Structure Resource (RCSR), including 1D ribbon structure, and 2D structures similar to **sql** or **kgm** topology. After considering these possible stacking models of eclipsed (AA) and staggered (AB) structures, the detailed simulation clearly suggested that the



Scheme 1. Schematic representation of hygroscopic COFs for photocatalytic H₂ evolution from water vapor.

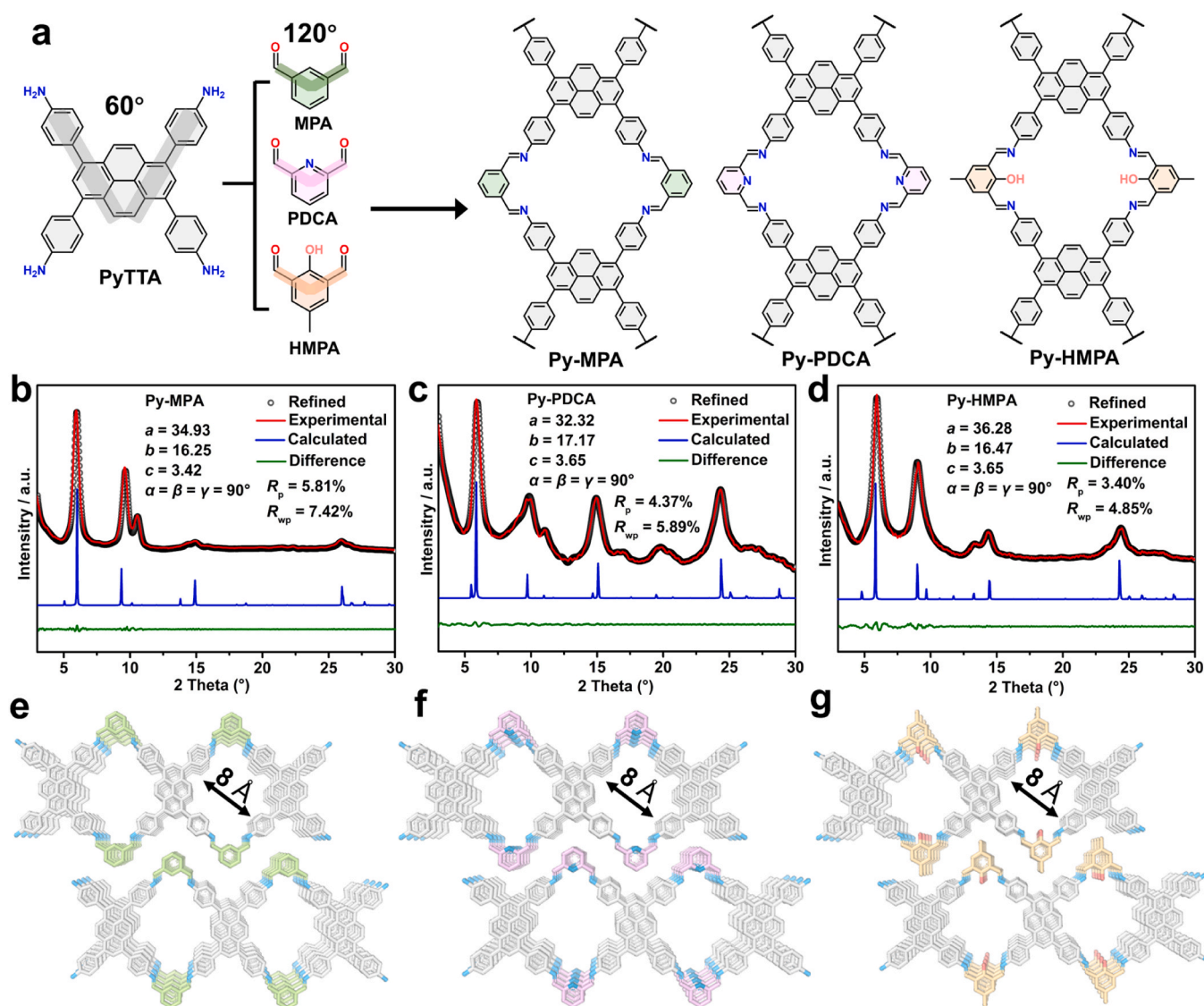


Fig. 1. (a) Synthesis and molecular structure of Py-MPA, Py-PDCA and Py-HMPA. Experimental, calculated and refined PXRD patterns of (b) Py-MPA, (c) Py-PDCA and (d) Py-HMPA. Top view of the structure for (e) Py-MPA, (f) Py-PDCA and (g) Py-HMPA.

three Py-COFs adopt 1D-AA structure (Figs. S13-S15). The V-shaped MPA, PDCA and HMPA with different potential water absorption sites were complementary to the 60° angles between the amino groups of Py, resulting in the formation of a four-membered micropore of about 8 Å, and then extended to be a ribbon structure (Fig. 1e-g). All Py-COFs are arranged in tightly zig-zag staggered arrangement resulting in abundant photosensitive Py units with strong π - π interactions, which facilitated the generation and transfer of photogenerated carriers.

The permanent porosity of the three COFs were evaluated by N₂ adsorption experiments. As shown in Fig. 2a-c, all the nitrogen isotherms exhibited sharp adsorption at low relative pressures, indicating the presence of abundant micropores. The Brunauer–Emmett–Teller (BET) surface area of Py-MPA, Py-PDCA and Py-HMPA were calculated to be 604, 643 and 705 m² g⁻¹, respectively. Moreover, nonlocal density functional theory (NLDFT) calculations revealed narrow pore size distribution of 0.77, 0.78 and 0.75 nm, which approached the theoretical pore size of Py-MPA, Py-PDCA and Py-HMPA with AA-1D structure. The formation of 1D ribbon-like Py-COFs was further confirmed by nitrogen sorption analysis.

The scanning electron microscopy (SEM) images indicated that the Py-COFs exhibited flower-like sheet morphology (Fig. S16). The

transmission electron microscopy (TEM) images displayed the nano-sheet morphology with dendritic nanoribbons, and the obvious lattice fringes further confirm the high crystallinity of Py-COFs (Fig. S17). The distance of the lattice spacings in three COFs were around 0.3 nm, which could be assigned to the (001) planes. The structural and thermal stability of the three COFs were further investigated. After soaking COFs in different solvents for 72 h, the PXRD patterns and FT-IR spectra of the treated COFs were maintained, indicating good structural stability (Figs. S18-S20). Thermogravimetric analysis (TGA) showed that the Py-COFs are thermally stable at high temperatures up to 500 °C (Figs. S21-S23).

Interestingly, when exposed to air, the dry Py-PDCA and Py-HMPA (drying temperature 100 °C) showed a color change from brown to red, while Py-MPA changed from pale yellow to deep yellow, indicating that COFs can adsorb water molecules in air as confirmed by FT-IR. Meanwhile, when temperatures up to 100 °C in TGA, Py-MPA, Py-PDCA and Py-HMPA showed a significant weight loss of 4.7, 10.4 and 16.7 wt% respectively, which indicated the loss of adsorbed water. Furthermore, the contact angle measurements were conducted to verify the surface hydrophilicity of Py-COFs, which was also an important factor affecting photocatalytic activities (Fig. S24). Py-HMPA and PDCA

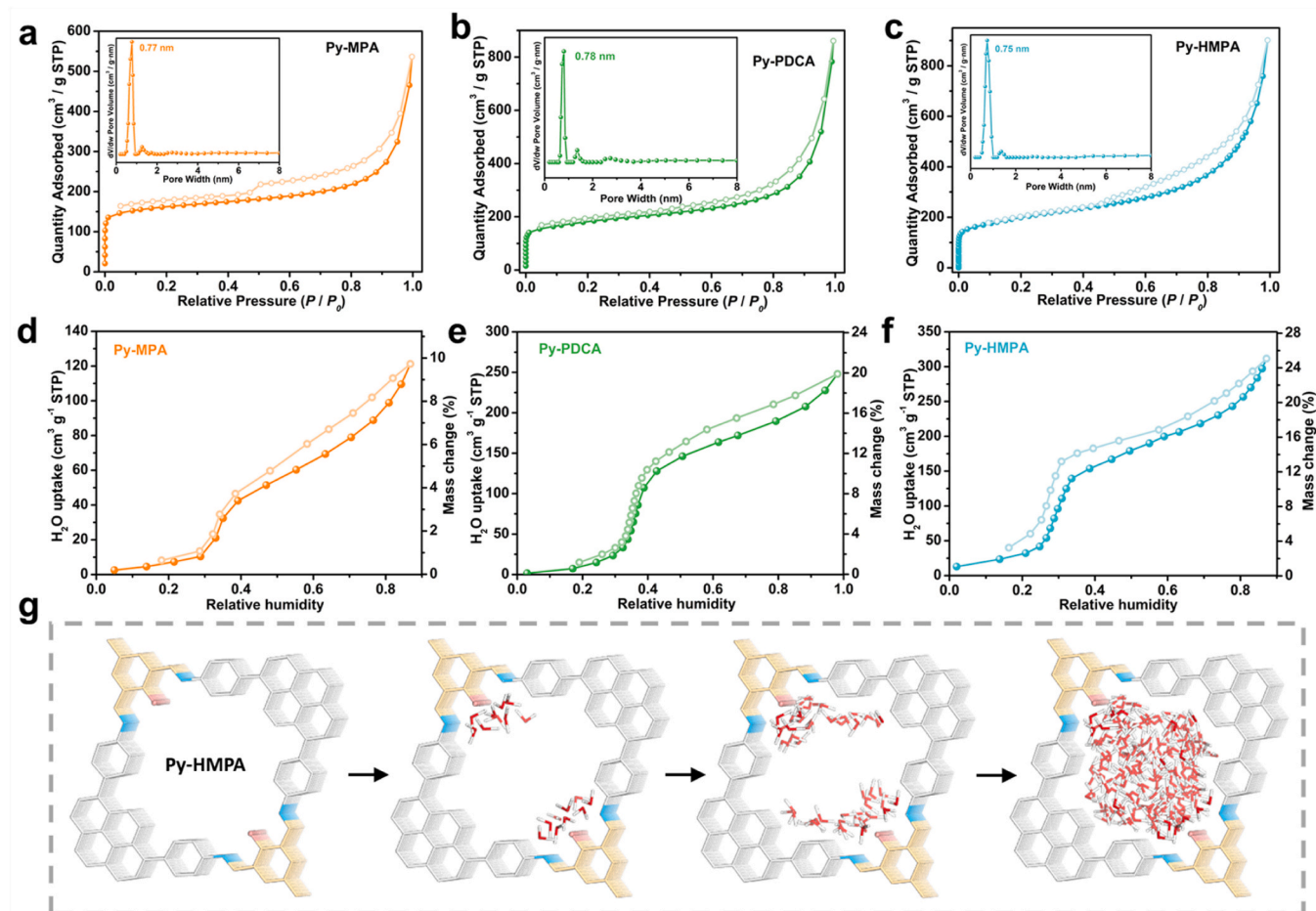


Fig. 2. N_2 adsorption/desorption isotherms and pore size distribution (inside) of (a) Py-MPA, (b) Py-PDCA and (c) Py-HMPA. Water vapor adsorption / desorption isotherms of (d) Py-MPA, (e) Py-PDCA and (f) Py-HMPA. (g) The simulated water adsorption behaviour of Py-HMPA.

exhibited a smaller contact angle (55° and 60°) than that of Py-MPA (70°), which may be attributed to the stronger hydrophilicity of pyridine and -OH groups.

Hence, water vapor adsorption experiments were carried out to quantify the water harvesting capacity of Py-COFs (Beishide Instrument Technology(Beijing) Co., Ltd, BSD-PMV2). The water vapor sorption isotherms measured at 298 K are both S-shaped isotherms (Fig. 2d-f), which are necessary for the adsorbent to absorb water under specific relative humidity (RH). Py-HMPA exhibited lower starting sorption inflection point around RH = 0.25 than Py-MPA (RH = 0.32) and Py-PDCA (RH = 0.28). It's well known that the adsorption process is first caused by the nucleation of water molecules at the absorption site [31], so the advanced adsorption inflection point of Py-HMPA proved that -OH sites within the pore channel was more hydrophilic compared to the pyridine group in Py-PDCA and phenyl group in Py-MPA. In addition, the obvious hysteresis loop of Py-HMPA at low humidity was also attributed to the incomplete desorption due to the strong adsorption ability of hydrophilic -OH sites. More importantly, Py-HMPA showed the highest total adsorption capacity ($311 \text{ cm}^3 \text{ g}^{-1}$) compared to Py-PDCA ($248 \text{ cm}^3 \text{ g}^{-1}$) and Py-MPA ($121 \text{ cm}^3 \text{ g}^{-1}$), demonstrating that the -OH-rich hydrophilic sites of Py-HMPA facilitated the adsorption and retention of water molecules in 1D channel. The water adsorption behavior of Py-COFs was further simulated using force-field-based grand-canonical Monte Carlo (GCMC) approach (Figs. S25 and S26). In the case of Py-HMPA (Fig. 2g), the snapshots revealed three stages of water adsorption process: i) water molecules are preferentially nucleated at the -OH sites in HMPA; ii) water molecules start to fill between the diagonals of the 1D pore channels; iii) water clusters continue to grow until the pore channels are

completely filled.

3.2. Photocatalytic hydrogen evolution reaction

UV/Vis diffuse reflectance spectra showed that Py-MPA exhibited an optical absorbance with the edge at 540 nm, while Py-PDCA and Py-HMPA presented apparent red shifts with a broadly intense absorbance at 600 and 650 nm, respectively (Fig. 3a). The optical band gaps of Py-MPA, Py-PDCA and Py-HMPA were calculated to be 2.31, 2.05 and 1.95 eV by Tauc plots, respectively, indicating that pyridine and -OH groups could narrow the band gap, thus increasing the light trapping ability. Furthermore, the conduction band (CB) positions of Py-MPA, Py-PDCA and Py-HMPA were estimated by electrochemical Mott-Schottky plots to be -0.39 , -0.42 and -0.51 (eV vs NHE), respectively (Figs. S27-S29). Combined with the band gap energy, the valence band (VB) positions of Py-MPA, Py-PDCA and Py-HMPA were 1.92, 1.63 and 1.44 eV vs. NHE, respectively (Fig. 3b) [32,33]. Notably, the above UV-Vis spectrum/Tauc plot of Py-COFs represent the post-water absorption state. Prior to water absorption, Py-COFs exhibited narrower light absorption, wider band gap, and larger VB (Fig. S30), suggesting Py-COFs subsequent to AWH are more favorable for photocatalytic processes. Based on the energy band structure of Py-COFs, the photocatalytic reduction of H_2O to H_2 and the oxidation of sacrificial electron donor ascorbic acid (H_2A) were thermodynamically allowed.

To investigate the photogenerated charge separation properties, photoluminescence (PL) spectroscopy and time-resolved PL decay measurements were conducted. As shown in Fig. 3c, Py-MPA displayed an intense fluorescence signal, which was substantially reduced and red-

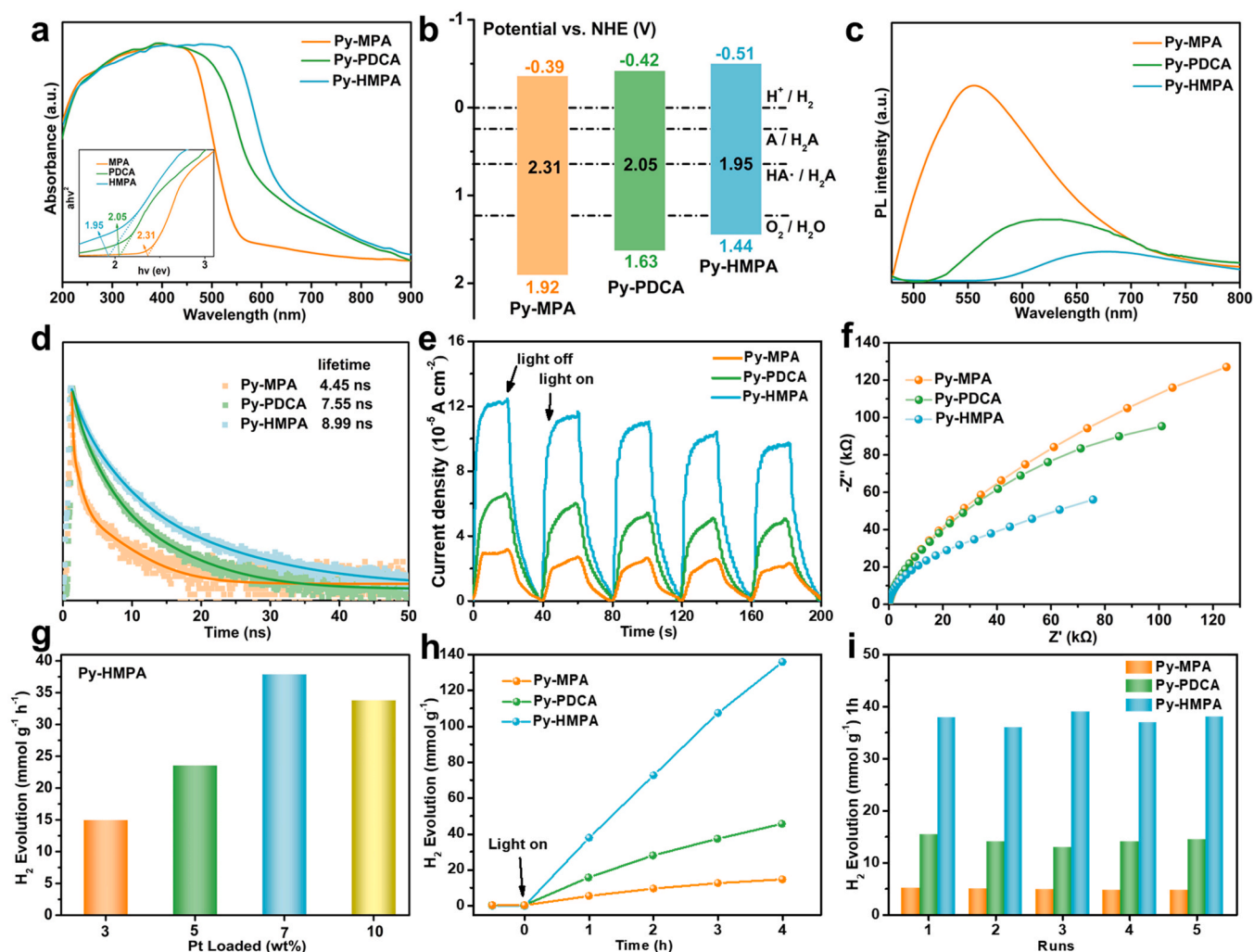


Fig. 3. (a) UV-vis spectra / Tauc plots, (b) Electronic band structure (c) PL spectra with the excitation wavelength at 405 nm, (d) Time-resolved PL decay curves, (e) Transient photocurrents and (f) Nyquist plots of three COFs. (g) The H_2 evolution in liquid water for Py-HMPA with different Pt loading amount. (h) Time dependent H_2 production in liquid water of three COFs. (i) The recycle ability of photocatalytic H_2 production in liquid water for three COFs.

shifted for Py-PDCA and Py-HMPA. Furthermore, the exciton binding energy (E_b) of Py-HMPA was evaluated to be 98 meV from temperature-dependent PL spectra (Fig. S31), which was much lower than Py-MPA (136 meV) and Py-PDCA (110 meV). Those results indicated that the introduction of pyridine and -OH groups may promote the separation of electrons and holes, which were further confirmed by increased charge carrier lifetimes for Py-PDCA (7.55 ns) and Py-HMPA (8.99 ns), as compared to Py-MPA (4.45 ns) (Fig. 3d) [34]. Moreover, compared to Py-MPA, the transient photocurrents of Py-PDCA and Py-HMPA were significantly enhanced, indicating the fast photoresponse (Fig. 3e). Additionally, the reduced resistance in impedance spectroscopy (EIS) also suggested that the charge transfer barrier was reduced with increased charge density in Py-PDCA and Py-HMPA (Fig. 3f) [35,36]. The slight decrease in photocurrent could be attributed to the equilibrium established between electrolyte solution and ITO electrode coated by the COFs layer during irradiation. These observations suggested the effective charge separation in Py-PDCA and Py-HMPA compared to Py-MPA, which should be beneficial for photocatalytic H_2 evolution.

After confirming the structures and photophysical properties of Py-COFs, the photocatalytic H_2 evolution was investigated in aqueous solution, with Pt served as co-catalyst and H_2A as sacrificial agent. As shown in Fig. 3g, the photocatalytic hydrogen evolution rate (HER) of Py-HMPA reached the highest value of $37925 \mu mol g^{-1} h^{-1}$ at 7 wt% Pt, which is higher than most COF-based photocatalysts (Table S1). The

activity declined with a loading of 10 wt% Pt, which might be due to light shielding by the deposited Pt. Meanwhile, the highest calculated apparent quantum yield (AQY) of Py-HMPA was 7.9% at 420 nm (Fig. S33). In addition, the HER of Py-HMPA and Py-PDCA ($15,450 \mu mol g^{-1} h^{-1}$) were much higher than that of Py-MPA ($5166 \mu mol g^{-1} h^{-1}$) at 7 wt% Pt loading (Fig. 3h), demonstrating that the introduction of pyridine and -OH groups in Py-COFs skeleton can enhance the photocatalytic activity. The long-term and recycling experiment of Py-COFs showed no obvious decline in H_2 production rate (Fig. 3i, S34), while the FT-IR spectra and PXRD patterns were well maintained after photocatalysis (Fig. S35), suggesting the good reaction stability. Next, the TEM images showed Pt nanoparticles were uniformly dispersed (Fig. S36), while the size of the Pt nanoparticles was concentrated around 4 nm. In addition, the ICP measurements of three COFs revealed that the actual Pt loading amount was determined by around 6 wt%. The Pt 4f XPS spectra could be resolved into two peaks corresponding to Pt^0 (Fig. S37) [27]. Interestingly, Py-HMPA with photodeposited Pt (Py-HMPA@Pt) still absorbed water from atmosphere (Fig. S38).

Considering its excellent AWH and photocatalytic performance, Py-HMPA@Pt was further investigated for H_2 production from water vapor. As shown in Fig. 4a, Py-HMPA@Pt mixed with H_2A was coated on the top of glass column and positioned into a typical top-illuminated photoreactor with circulating condensate water. Crucially, deionized water was added around the glass column inside the reactor, which

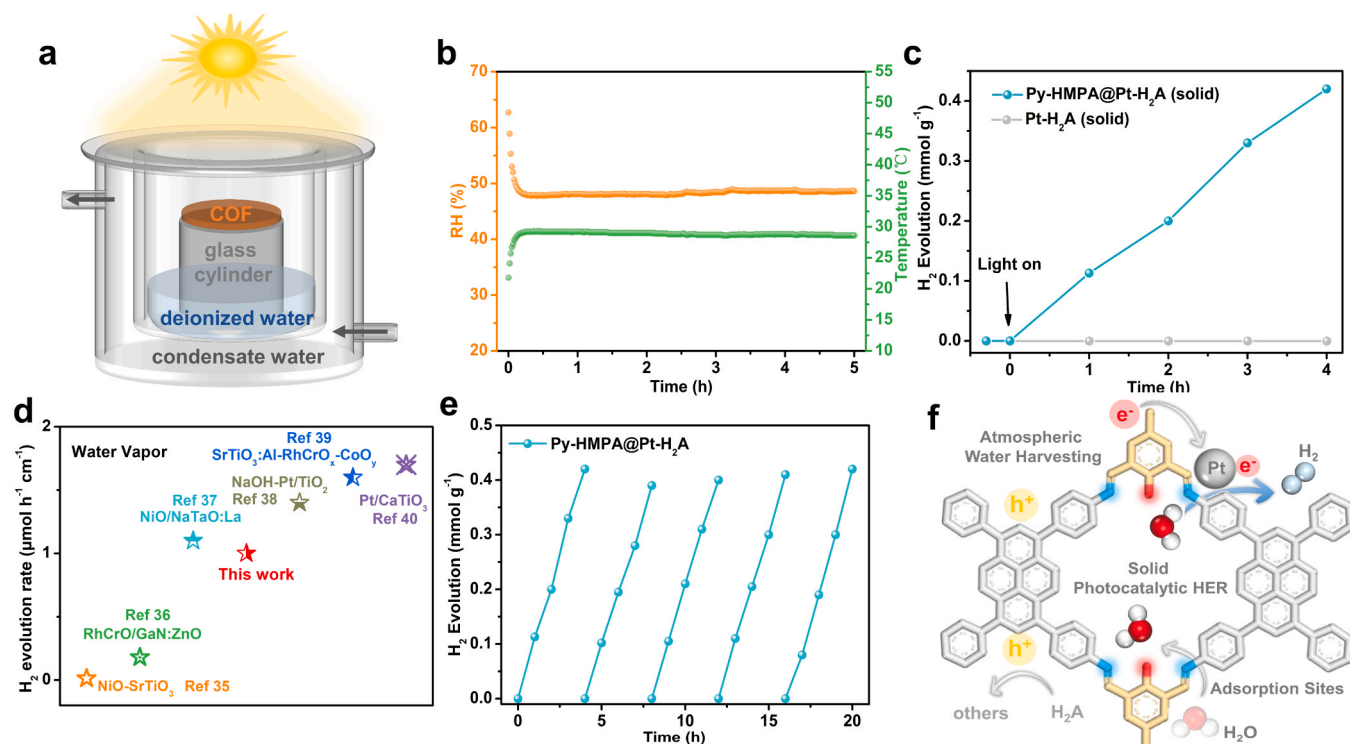


Fig. 4. (a) Schematic diagram of photocatalytic water vapor splitting system. (b) The relative temperature and humidity in water vapor photoreactor. (c) Time dependent H_2 production of solid Py-HMPA@Pt. (d) The comparison of photocatalytic water vapor splitting performance. (e) The recycle ability of photocatalytic H_2 production for Py-HMPA@Pt. (f) The mechanism for photocatalytic water vapor splitting on Py-HMPA@Pt.

served as the source of water vapor for photoreaction process. Before performing the solid photocatalysis, the hygromograph was introduced above the glass cylinder to record the time-dependent relative temperature and humidity in the photoreactor (Fig. S39). The temperature and humidity in the reactor reached 28 °C and 48% RH quickly within ten minutes of illumination (Fig. 4b), and remained stable for the next five hours under illumination, which was enough for Py-HMPA@Pt to collect water from the reactor according to the water adsorption curve. The temperature of COF surface was also monitored and revealed slightly higher than the temperature inside reactor (Fig. S40). Surprisingly, the solid photocatalytic HER of Py-HMPA@Pt was still remained 105 $\mu\text{mol g}^{-1} \text{h}^{-1}$ under water vapor conditions with only 48 RH% (Fig. 4c, S41). Meanwhile, the calculated AQY of Py-HMPA@Pt was 0.51% at 420 nm under water vapor. We acknowledge that the activity of various materials was difficult to compare due to the different reaction conditions. The reported inorganic materials for photocatalytic water vapor splitting were mostly fed under saturated H_2O vapor at several atmospheric pressures, whereas Py-HMPA realizes AWH at normal atmospheric pressure with low humidity (RH = 0.48). Moreover, the performance of Py-HMPA@Pt after unit conversion (1.0 $\mu\text{mol h}^{-1} \text{cm}^{-1}$) was still comparable to the inorganic materials (Fig. 4d) [37–42]. More importantly, the HER (Fig. 4e) and crystallinity (Fig. S42) of Py-HMPA@Pt were well maintained after several cycles, suggesting good photocatalytic stability.

To gain more insight into the catalytic mechanism on hydrogen evolution of hygroscopic Py-COFs, DFT calculations were performed [43–45]. The electrostatic potential surfaces showed that -OH groups of Py-HMPA with the most negative electrostatic potential would promote the separation of electrons/holes and the formation of hydrogen bond with H_2O [44], comparing to the phenyl unit of Py-MPA and pyridyl unit of Py-PDCA (Fig. S43). Furthermore, H_2O adsorption energies were calculated and analyzed to conclude that the -OH groups of Py-HMPA possessed the lowest adsorption energy for H_2O , thus leading to the easier nucleation of water at -OH sites, followed by the formation of

water clusters through hydrogen bonding interaction, and eventually leading to the lower starting point of water vapor adsorption (Fig. S44). In addition, the highest occupied molecular orbital (HOMO) of the three COFs were all localized on the pyrene units, suggesting the sites of photogenerated holes (Fig. S45) [45]. The lowest unoccupied molecular orbital (LUMO) of Py-MPA, Py-PDCA and Py-HMPA were localized on the phenyl, pyridyl and p-methylphenol groups respectively, proving the sites of photogenerated electrons. And then electrons transferred to the Pt^0 deposited on COFs.

Based on above experiments and theoretical calculations, the mechanism for solid photocatalytic H_2 evolution on Py-HMPA was showed in Fig. 4f. Firstly, the atmospheric water harvesting was started, and water molecules were adsorbed into internal structure of hygroscopic Py-HMPA. Meanwhile, the photoexcitation of Py-HMPA by photons led to the localization of photogenerated e^- and h^+ at p-methylphenol unit and pyrene unit, respectively. Immediately, photogenerated electrons transfer to the surface Pt^0 cocatalyst, and then reduced the water molecules into H_2 , with H_2A as sacrificial agents consuming the photogenerated holes.

4. Conclusions

In summary, three hygroscopic 1D COFs were rationally designed to achieve efficient photocatalytic H_2 evolution from water vapor by integrating AWH and photocatalysis. The photosensitive pyrene unit is prerequisite for the efficient photocatalysis of Py-COFs. 1D skeleton structure with ultra-small pore channels is essential for AWH to satisfy the micropore filling of water molecules. The appropriate hydrophilic groups such as -OH not only promote the rapid nucleation of water molecules but also enhance the separation of photogenerated charges. To the best of our knowledge, this study demonstrates the first example of COFs for photocatalytic water vapor splitting, presenting a new strategy for solar-to-hydrogen conversion.

CRediT authorship contribution statement

Yong Liu: Conceptualization, Methodology, Validation, Investigation, Writing – original draft, Writing – review & editing. **Wang-Kang Han:** Validation, Writing – original draft. **Wenwen Chi:** Resources, Investigation. **Jia-Xing Fu:** Resources, Investigation. **Yuqian Mao:** Investigation. **Xiaodong Yan:** Writing – review & editing. **Jun-Xiang Shao:** Writing – review & editing. **Yuqin Jiang:** Supervision. **Zhi-Guo Gu:** Supervision, Project administration, Funding acquisition.

Declaration of Competing Interest

The authors declare that they have no known competing financial interests or personal relationships that could have appeared to influence the work reported in this paper.

Data Availability

Data will be made available on request.

Acknowledgements

This work was supported by the National Natural Science Foundation of China (22075108, 21905116), the Open Research Fund of School of Chemistry and Chemical Engineering, Henan Normal University (2022B01) and Postgraduate Research & Practice Innovation Program of Jiangsu Province (KYCX23_2464).

Appendix A. Supporting information

Supplementary data associated with this article can be found in the online version at [doi:10.1016/j.apcatb.2023.123074](https://doi.org/10.1016/j.apcatb.2023.123074).

References

- [1] E. Nikoloudakis, I. Lopez-Duarte, G. Charalambidis, K. Ladomenou, M. Ince, A. G. Coutsolelos, Porphyrins and phthalocyanines as biomimetic tools for photocatalytic H₂ production and CO₂ reduction, *Chem. Soc. Rev.* 51 (2022) 6965–7045.
- [2] T. Takata, J. Jiang, Y. Sakata, M. Nakabayashi, N. Shibata, V. Nandal, K. Seki, T. Hisatomi, K. Domen, Photocatalytic water splitting with a quantum efficiency of almost unity, *Nature* 581 (2020) 411–414.
- [3] Q. Wang, K. Domen, Particulate photocatalysts for light-driven water splitting: mechanisms, challenges, and design strategies, *Chem. Rev.* 120 (2020) 919–985.
- [4] H. Nishiyama, T. Yamada, M. Nakabayashi, Y. Maehara, M. Yamaguchi, Y. Kuroki, Y. Nagatsuma, H. Tokudome, S. Akiyama, T. Watanabe, R. Narushima, S. Okunaka, N. Shibata, T. Takata, T. Hisatomi, K. Domen, Photocatalytic solar hydrogen production from water on a 100 m² scale, *Nature* 598 (2021) 304–307.
- [5] T. Takata, C. Pan, M. Nakabayashi, N. Shibata, K. Domen, Fabrication of a core-shell-type photocatalyst via photodeposition of group IV and V transition metal oxyhydroxides: an effective surface modification method for overall water splitting, *J. Am. Chem. Soc.* 137 (2015) 9627–9634.
- [6] G.N. Schrauzer, T.D. Guth, Photolysis of water and photoreduction of nitrogen on titanium dioxide, *J. Am. Chem. Soc.* 99 (1977) 7189–7193.
- [7] M. Schreck, M. Niederberger, Photocatalytic gas phase reactions, *Chem. Mater.* 31 (2019) 597–618.
- [8] T. Suguro, F. Kishimoto, K. Takanabe, Photocatalytic hydrogen production under water vapor feeding—a minireview, *Energy Fuels* 36 (2022) 8978–8994.
- [9] H. Han, K. Huang, Y. Yao, Z. Li, X. Meng, Enhanced photocatalytic splitting of photothermally induced water vapor to evolve hydrogen, *Chem. Eng. J.* 450 (2022), 138419.
- [10] J.-C. Wang, Y. Hou, F.-D. Feng, W.-X. Wang, W. Shi, W. Zhang, Y. Li, H. Lou, C.-X. Cui, A recyclable molten-salt synthesis of B and K co-doped g-C₃N₄ for photocatalysis of overall water vapor splitting, *Appl. Surf. Sci.* 537 (2021), 148014.
- [11] L. Yang, S.K. Ravi, D.K. Nandakumar, F.I. Alzakia, W. Lu, Y. Zhang, J. Yang, Q. Zhang, X. Zhang, S.C. Tan, A hybrid artificial photocatalysis system splits atmospheric water for simultaneous dehumidification and power generation, *Adv. Mater.* 31 (2019), e1902963.
- [12] Y.-N. Gong, X. Guan, H.-L. Jiang, Covalent organic frameworks for photocatalysis: synthesis, structural features, fundamentals and performance, *Coord. Chem. Rev.* 475 (2023), 214889.
- [13] W.K. Han, Y. Liu, X. Yan, Y. Jiang, J. Zhang, Z.G. Gu, Integrating light-harvesting ruthenium(II)-based units into three-dimensional metal covalent organic frameworks for photocatalytic hydrogen evolution, *Angew. Chem. Int. Ed.* 61 (2022), e202208791.
- [14] S. Liu, M. Wang, Y. He, Q. Cheng, T. Qian, C. Yan, Covalent organic frameworks towards photocatalytic applications: design principles, achievements, and opportunities, *Coord. Chem. Rev.* 475 (2023), 214882.
- [15] Y. Liu, W.-K. Han, W. Chi, Y. Mao, Y. Jiang, X. Yan, Z.-G. Gu, Substoichiometric covalent organic frameworks with uncondensed aldehyde for highly efficient hydrogen peroxide photosynthesis in pure water, *Appl. Catal. B Environ.* 331 (2023), 122691.
- [16] H. Wang, H. Wang, Z. Wang, L. Tang, G. Zeng, P. Xu, M. Chen, T. Xiong, C. Zhou, X. Li, D. Huang, Y. Zhu, Z. Wang, J. Tang, Covalent organic framework photocatalysts: structures and applications, *Chem. Soc. Rev.* 49 (2020) 4135–4165.
- [17] R. Chen, Y. Wang, Y. Ma, A. Mal, X.Y. Gao, L. Gao, L. Qiao, X.B. Li, L.Z. Wu, C. Wang, Rational design of isostructural 2D porphyrin-based covalent organic frameworks for tunable photocatalytic hydrogen evolution, *Nat. Commun.* 12 (2021) 1354.
- [18] B. Gui, H. Ding, Y. Cheng, A. Mal, C. Wang, Structural design and determination of 3D covalent organic frameworks, *Trends Chem.* 4 (2022) 437–450.
- [19] L.H. Chen, W.K. Han, X. Yan, J. Zhang, Y. Jiang, Z.G. Gu, A highly stable ortho-ketoneamine covalent organic framework with balanced hydrophilic and hydrophobic sites for atmospheric water harvesting, *ChemSusChem* 15 (2022), e202201824.
- [20] H. Lu, W. Shi, Y. Guo, W. Guan, C. Lei, G. Yu, Materials engineering for atmospheric water harvesting: progress and perspectives, *Adv. Mater.* 34 (2022), e2110079.
- [21] H.L. Nguyen, N. Hanikel, S.J. Lyle, C. Zhu, D.M. Proserpio, O.M. Yaghi, A. Porous, Covalent organic framework with voided square grid topology for atmospheric water harvesting, *J. Am. Chem. Soc.* 142 (2020) 2218–2221.
- [22] C. Sun, Y. Zhu, P. Shao, L. Chen, X. Huang, S. Zhao, D. Ma, X. Jing, B. Wang, X. Feng, 2D covalent organic framework for water harvesting with fast kinetics and low regeneration temperature, *Angew. Chem. Int. Ed.* 62 (2023), e202217103.
- [23] Y. Hu, Z. Ye, X. Peng, Metal-organic frameworks for solar-driven atmosphere water harvesting, *Chem. Eng. J.* 452 (2023), 139656.
- [24] N. Hanikel, X. Pei, S. Chheda, H. Lyu, W. Jeong, J. Sauer, L. Gagliardi, O.M. Yaghi, Evolution of water structures in metal-organic frameworks for improved atmospheric water harvesting, *Science* 374 (2021) 454–459.
- [25] J.C. Wagner, K.M. Hunter, F. Paesani, W. Xiong, Water capture mechanisms at zeolitic imidazolate framework interfaces, *J. Am. Chem. Soc.* 143 (2021) 21189–21194.
- [26] S.S. Zhao, J. Liang, D.-H. Si, M.-J. Mao, Y.B. Huang, R. Cao, Superheterojunction covalent organic frameworks: supramolecular synergetic charge transfer for highly efficient photocatalytic CO₂ reduction, *Appl. Catal. B Environ.* 333 (2023), 122782.
- [27] Y. Li, L. Yang, H. He, L. Sun, H. Wang, X. Fang, Y. Zhao, D. Zheng, Y. Qi, Z. Li, W. Deng, In situ photodeposition of platinum clusters on a covalent organic framework for photocatalytic hydrogen production, *Nat. Commun.* 13 (2022) 1355.
- [28] S. An, X. Li, S. Shang, T. Xu, S. Yang, C.X. Cui, C. Peng, H. Liu, Q. Xu, Z. Jiang, J. Hu, One-dimensional covalent organic frameworks for the 2e⁻ oxygen reduction reaction, *Angew. Chem. Int. Ed.* (2023), e202218742.
- [29] Z. Chen, K. Wang, Y. Tang, L. Li, X. Hu, M. Han, Z. Guo, H. Zhan, B. Chen, Reticular synthesis of one-dimensional covalent organic frameworks with 4-c sq topology for enhanced fluorescence emission, *Angew. Chem. Int. Ed.* (2022), e202213268.
- [30] H.L. Nguyen, C. Gropp, O.M. Yaghi, Reticulating 1D ribbons into 2D covalent organic frameworks by imine and imide linkages, *J. Am. Chem. Soc.* 142 (2020) 2771–2776.
- [31] M.J. Kalmutzki, C.S. Diercks, O.M. Yaghi, Metal-organic frameworks for water harvesting from air, *Adv. Mater.* 30 (2018), e1704304.
- [32] H. Cheng, H. Lv, J. Cheng, L. Wang, X. Wu, H. Xu, 35 Rational design of covalent heptazine frameworks with spatially separated redox centers for high-efficiency photocatalytic hydrogen peroxide production, *Adv. Mater.* 34 (2022), e2107480.
- [33] L. Hao, R. Shen, C. Huang, Z. Liang, N. Li, P. Zhang, X. Li, C. Qin, X. Li, Fluorenone-based covalent organic frameworks with efficient exciton dissociation and well-defined active center for remarkable photocatalytic hydrogen evolution, *Appl. Catal. B Environ.* 330 (2023), 122581.
- [34] C. Wu, Z. Teng, C. Yang, F. Chen, H.B. Yang, L. Wang, H. Xu, B. Liu, G. Zheng, Q. Han, Polarization engineering of covalent triazine frameworks for highly efficient photosynthesis of hydrogen peroxide from molecular oxygen and water, *Adv. Mater.* 34 (2022), e2110266.
- [35] J.N. Chang, Q. Li, J.W. Shi, M. Zhang, L. Zhang, S. Li, Y. Chen, S.L. Li, Y.Q. Lan, Oxidation-reduction molecular junction covalent organic frameworks for full reaction photosynthesis of H₂O₂, *Angew. Chem. Int. Ed.* 62 (2023), e202218868.
- [36] X. Zhong, Q. Ling, Z. Ren, B. Hu, Immobilization of U(VI) onto covalent organic frameworks with the different periodic structure by photocatalytic reduction, *Appl. Catal. B Environ.* 326 (2023), 122398.
- [37] K. Domen, S. Naito, M. Soma, T. Onishi, K. Tamaru, Photocatalytic decomposition of water vapour on an NiO–SrTiO₃ catalyst, *J. Chem. Soc., Chem. Commun.* 12 (1980) 543–544.
- [38] F. Dionigi, P.C.K. Vesborg, T. Pedersen, O. Hansen, S. Dahl, A. Xiong, K. Maeda, K. Domen, I. Chorkendorff, Gas phase photocatalytic water splitting with Rh₂-yCr₂O₃/Ga₂N:ZnO in μ-reactors, *Energy Environ. Sci.* 4 (2011) 2937–2942.
- [39] K. Shimura, S. Kato, T. Yoshida, H. Itoh, T. Hattori, H. Yoshida, Photocatalytic steam reforming of methane over sodium tantalate, *J. Phys. Chem. C* 114 (2010) 3493–3503.
- [40] S. Sato, J.M. White, Photocatalytic water decomposition and water-gas shift reactions over NaOH-coated, platinumized TiO₂, *J. Catal.* 69 (1981) 128–139.

- [41] C.J. Shearer, T. Hisatomi, K. Domen, G.F. Metha, Gas phase photocatalytic water splitting of moisture in ambient air: Toward reagent-free hydrogen production, *J. Photochem. Photobiol. A Chem.* 401 (2020), 112757.
- [42] K. Shimura, H. Yoshida, 6 Hydrogen production from water and methane over Pt-loaded calcium titanate photocatalyst, *Energy Environ. Sci.* 3 (2010) 615–617.
- [43] X. Zhang, P. Ma, C. Wang, L. Gan, X. Chen, P. Zhang, Y. Wang, H. Li, L. Wang, X. Zhou, K. Zheng, Unraveling the dual defect sites in graphite carbon nitride for ultra-high photocatalytic H₂O₂ evolution, *Energy Environ. Sci.* 15 (2022) 830–842.
- [44] Z. You, B. Wang, Z. Zhao, Q. Zhang, W. Song, C. Zhang, X. Long, Y. Xia, Metal-free carbon-based covalent organic frameworks with heteroatom-free units boost efficient oxygen reduction, *Adv. Mater.* 35 (2022) 2209129.
- [45] L. Wang, R. Lian, Y. Zhang, X. Ma, J. Huang, H. She, C. Liu, Q. Wang, Rational preparation of cocoon-like g-C₃N₄/COF hybrids: accelerated intramolecular charge delivery for photocatalytic hydrogen evolution, *Appl. Catal. B Environ.* 315 (2022), 121568.